Journal of Power Sources 205 (2012) 129–135

Contents lists available at SciVerse ScienceDirect

Journal of Power Sources

journal homepage: www.elsevier.com/locate/jpowsour

Synthesis and properties of Fe_3O_4/polyaniline and its tiny magnetic field functions during oxygen transfer processes

Jicheng Shi, Hongfeng Xu*, Hong Zhao, Lu Lu

College of Environmental and Chemical Engineering, Dalian Jiaotong University, Dalian 116028, Liaoning Province, PR China

ARTICLE INFO

Article history:
Received 16 November 2011
Accepted 2 January 2012
Available online 10 January 2012

Keywords:
Magnetic field
Oxygen transfer
Zinc air fuel cell
Electric double-layer capacitance
Charge-transfer resistance

ABSTRACT

The promotion of oxygen transfer by tiny magnetic fields has a great theoretical and practical significance in the improvement of fuel cell performance. In the present study, a Fe_3O_4/polyaniline (PANI) material is prepared via sol–gel and in situ polymerization. The structures of Fe_3O_4, PANI, and Fe_3O_4/PANI are characterized via X-ray diffraction, Fourier transform infrared spectroscopy, scanning electron microscopy, vibrating sample magnetometry, and differential thermal analysis. A three-electrode electrochemical device and zinc air fuel cells (ZAFC) are used to investigate the functions of Fe_3O_4/PANI during the oxygen transfer process. The conductivity of Fe_3O_4/PANI is 0.30 S cm^{-1}, the intrinsic coercivity is 10.18 kA m^{-1}, and the remanent magnetization is 5.27 A m^2 kg^{-1}. At a low Fe_3O_4/PANI load density, the tiny magnetic field can promote oxygen transfer, increase the electric double-layer capacitance, lower the charge-transfer resistance, and improve the ZAFC discharge performance. At a high load density of 7.11 mg cm^{-2}, the tiny magnetic field can inhibit oxygen transfer because of the interactions between the different magnetic poles. Fe_3O_4/PANI can also improve the ZAFC discharge performance under nonmagnetic conditions because of its higher electrochemical reduction activities.

1. Introduction

Fuel cells can directly convert chemical energy into electric energy and have higher energy utilization capacities than traditional thermal engines. Fuel cells with various sizes have extended applications from micropowered devices to industrial purposes, including mobile and stationary applications. Atmospheric oxygen is the oxidant in the cathode of proton exchange membrane fuel cells (PEMFC) and zinc air fuel cells (ZAFC). Oxygen-transfer promotion in the cathode can further improve the discharge performance of fuel cells [1,2]. Increased air pressure can accelerate oxygen transfer, but the energy consumption and intensity requirements of bipolar plates can also be significantly increased. Based on the magnetic oxygen-enrichment theory, using a magnetic field to facilitate oxygen transfer can improve the fuel cell discharge performance.

Oxygen and nitrogen molecules have different magnetic flow behaviors in a magnetic field. Oxygen is paramagnetic, whereas nitrogen is diamagnetic. These two types of molecules have different magnetization intensities (M) in a gradient magnetic field (B). Thus, the magnetic forces (F) acting on nitrogen and oxygen molecules are in opposite directions. Therefore, a magnetic force can induce the separation and enrichment of oxygen and nitrogen molecules [3], as shown in Fig. 1.

Current-carrying solenoids, block-shaped permanent magnets, and nanoscale magnetic materials can all provide a magnetic field with a certain strength. However, the former two magnetic field sources affect the shape, size, and weight of fuel cells. Nanoscale magnetic materials are ideal for oxygen transfer in the PEMFC or ZAFC cathode. Fe_3O_4 is a spinel type of magnetic material that exhibits superparamagnetic or ferromagnetic properties, depending on the particle size and service temperatures [4,5]. Superparamagnetic Fe_3O_4 is already being applied in nucleic acid analysis, clinical diagnosis, drug targeting, enzyme and cell immobilization, and so on [6–8]. Ferromagnetic Fe_3O_4 has a definite coercivity (H_{ic}) and remanent magnetization (M_r), which can be applied to fuel cells to improve the discharge performance of PEMFC or ZAFC using the tiny magnetic field that Fe_3O_4 generates.

The surface of Fe_3O_4 nanoparticles requires modification because of the highly oxidizable and unstable properties of the nanoparticles in aqueous solutions [9–12]. The conductive polyaniline (PANI) can be used to coat Fe_3O_4 nanoparticles and enhance their conductivity and stability [13–15]. The present paper focuses on the preparation of Fe_3O_4/PANI materials and the study of their tiny magnetic field functions during oxygen-transfer processes in electrodes or ZAFC cathodes.

* Corresponding author. Tel.: +86 411 84106713; fax: +86 411 84106723.
E-mail address: hfxu@fuelcell.com.cn (H. Xu).

0378-7753/$ – see front matter © 2012 Elsevier B.V. All rights reserved.
doi:10.1016/j.jpowsour.2012.01.046

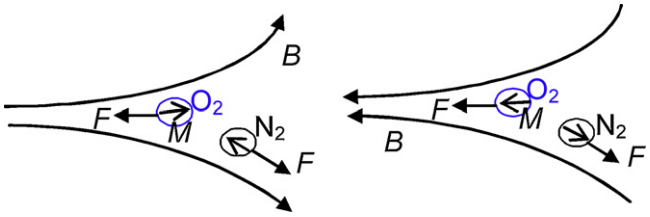

Fig. 1. Oxygen and nitrogen separation in a gradient magnetic field.

2. Experimental procedures

2.1. Synthesis of Fe_3O_4 and Fe_3O_4/PANI samples

Fe_3O_4 was synthesized under a 5 mT magnetic field. Same volumes of 0.05 M KOH and 0.2 M KNO_3 solutions were mixed under vigorous stirring. $FeSO_4$ (0.04 M), with a volume half that of KOH or KNO_3, was slowly dripped into the mixed solutions at 2 drops min^{-1}. The solution was then stirred and precipitated at 90 °C for 4 h in a water bath. The resulting black Fe_3O_4 gel was washed three to four times with deionized water. The sediment was dried in a vacuum at 80 °C, and the dried product was ground to obtain Fe_3O_4 magnetic powder.

Exactly 1 g Fe_3O_4 was added to a beaker containing 50 mL 1 M sulfosalicylic acid. The solution was quickly stirred, and 4 mL distilled aniline was poured into the solution. $(NH_4)_2S_2O_8$ (1 M) was dripped into the solution at a rate of 2 drops min^{-1} for 1 h. The product was then filtered and successively washed with 1 M HCl, 95% alcohol, and deionized water. The filter cake was dried at 100–110 °C and then ground to obtain Fe_3O_4/PANI magnetic powder.

2.2. Nanomaterial characterization

The X-ray diffraction (XRD) patterns of the samples were obtained using an X-ray diffractometer (D/max2400, Rigaku Co., Japan) with Cu Kα radiation (0.1542 nm) in the 2θ range of 6°–80°. The Fourier transform infrared (FT-IR) spectra of the samples in KBr tablets were recorded on an FT-IR spectrometer (FTIR430, Jasco Co., Japan). Magnetic hysteresis loops were measured using a vibrating sample magnetometer (JDM-13, Changchun Tongzhou Co., China). The conductivities of the samples were measured at room temperature using a digital four-probe resistance tester (SX1934, Shanghai Huayan Co., China), and the conductivity values were directly calculated from the measured resistance and sample dimensions. Thermogravimetric (TG), differential TG (DTG), and differential scanning calorimetric (DSC) analyses were performed on a differential thermal analyzer (STA449F3, Netzsch Co., Germany) in an Ar atmosphere at 35–1200 °C, at a heating rate of 10 K min^{-1}.

2.3. Three-electrode electrochemical measurements with Fe_3O_4/PANI in a graphite electrode

Electrochemical experiments were conducted in an electrochemical workstation (CHI660C, Shanghai Chenhua Co., China). A certain amount of Fe_3O_4/PANI, 50% Pt/C (Dalian Sunrise Power Co., China), and 5% Nafion (Dupont Co., USA) were homogeneously mixed via ultrasonication. The homogeneous solutions were loaded on the graphite sheet under a 350 mT magnetic field and served as the working electrode. Another blank graphite sheet served as the counter electrode, and a saturated calomel electrode (SCE) was used as the reference electrode. H_2SO_4 (0.5 M) was used as the electrolyte under continuous air saturation. After the magnetic particles and the Pt/C catalyst were loaded on the working electrode, the electrode was magnetized using a TSK-H1540 magnetizing machine (Nanjing Tingjin Co., China), thereby obtaining the magnetic electrode. An unmagnetized electrode, called the nonmagnetic electrode, was used for comparison. The electrochemical performance of Fe_3O_4/PANI and the effect of the tiny magnetic field on oxygen transfer were evaluated in a three-electrode glass cell through different measurements, namely, the small triangular waveform sweep from 0.80 V to 0.79 V (vs. SCE) at a scan rate of 100 V s^{-1}; the multi-current step with successive steps of −100, −10, −1, and −0.1 mA; the multi-potential steps between 1.0 V and 0.4 V (vs. SCE) at a step of −0.2 V each; and the Tafel test from 1 V to 0 V (vs. SCE) at a scan rate of 10 mV s^{-1}.

2.4. Discharge performance of ZAFC with Fe_3O_4/PANI in the cathode

The ZAFC anode consisted of a copper foil coated with a zinc paste (Zn:30% KOH:polyacrylic acid sodium = 5.99:4:0.01,w/w/w). The paste was first stirred and then set aside for 5 h. The copper foil loading area was 2.25 cm^2. The cathode was foamed nickel, which was loaded with a homogeneous mixture of Fe_3O_4/PANI, 50% Pt/C (0.4 mg cm^{-2}) and acetylene black (0.4 mg cm^{-2}) under a 350 mT magnetic field. The foamed nickel was placed in a vacuum-drying oven at 180 °C for 30 min. The cathode was then magnetized, and the magnetic cathode was obtained. A nonmagnetic cathode served as the blank control cathode. A hydrated cellulose membrane served as an intermediate layer between the anode and the cathode. The current collector was a copper plate, on one side of which ventilation holes were distributed. The discharge performance of ZAFC was evaluated using an electric charge/discharge instrument (CT2001A-2V-1A, Wuhan Landian Co., China).

3. Results and discussion

3.1. Structural characterization of Fe_3O_4, Fe_3O_4/PANI and PANI

Fig. 2 shows the XRD patterns of the Fe_3O_4, Fe_3O_4/PANI, and PANI materials. The diffraction peaks at 35.5°, 62.7°, 30.1°, 57.1°, 43.2°, and 18.3° (Fig. 2a), which are in the order of decreasing diffraction intensity, correspond to the (3 1 1), (4 4 0), (2 2 0), (5 1 1), (4 0 0), and (1 1 1) crystal planes of Fe_3O_4, respectively [16]. This result is consistent with the standard spectrum of JCPDS 88-0866, indicating that the synthesized Fe_3O_4 has a cubic spinel structure. Strong PANI diffraction peaks located at 27.4°, 13.2°, 17.6°, and 28.2° can also be seen in Fig. 2b. The crystallinity is 78.41%, as shown

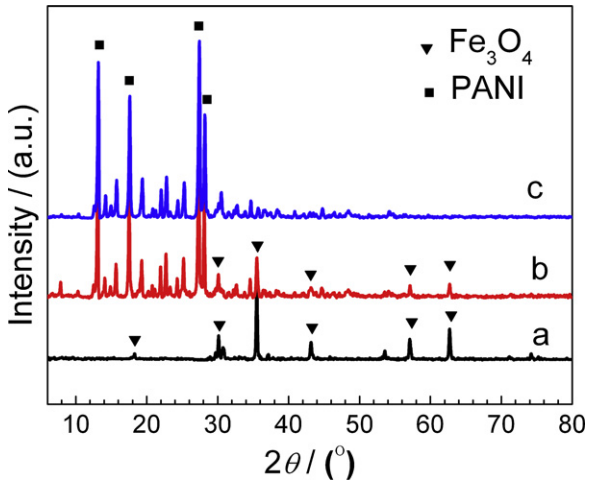

Fig. 2. X-ray diffraction (XRD) patterns of (a) Fe_3O_4, (b) Fe_3O_4/polyaniline (PANI), and (c) PANI.

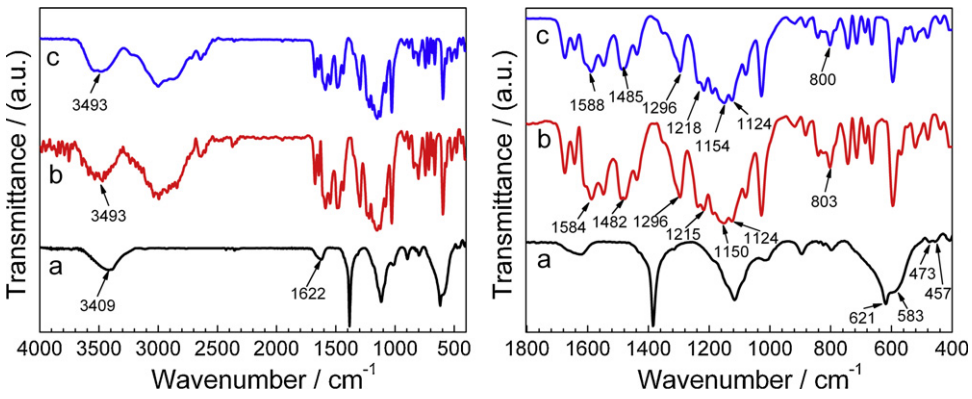

Fig. 3. FT-IR spectra of (a) Fe_3O_4, (b) Fe_3O_4/PANI, and (c) PANI.

in Fig. 2c [17–19]. These results prove that Fe_3O_4/PANI has a dual phase composition, namely, the Fe_3O_4 and PANI phases.

Fig. 3 shows the typical FT-IR spectra of Fe_3O_4, Fe_3O_4/PANI, and PANI. In Fig. 3a, the 3409 and 1622 cm^{-1} peaks are attributed to the —OH stretching vibration as well as the deformation vibration of H_2O resulting from moisture adsorption on the magnetic powder surface [20]. The characteristic peaks of Fe_3O_4 are at 621, 583, 473, and 457 cm^{-1}. The peaks at 621 and 583 cm^{-1} are assigned to the Fe^{3+}—O—Fe^{3+} and Fe^{2+}—O—Fe^{2+} symmetrical stretching vibrations, respectively. The Fe^{2+}—O—Fe^{2+} adsorption peak is located at the edge of the Fe^{3+}—O—Fe^{3+} peak. The 473 and 457 cm^{-1} peaks are attributed to the antisymmetric stretching vibrations of Fe^{3+}—O—Fe^{3+} and Fe^{2+}—O—Fe^{2+}, respectively. The characteristic peaks of the Fe—O bond of the Fe_3O_4 block material are at 570 and 375 cm^{-1} [21,22]. When the Fe_3O_4 particle size is reduced to the nanoscale, a large number of atoms become exposed to the surface. Thus, nonlocal electrons are rearranged, and the nanoscale size effects induce the bond force constant at the particle surfaces to increase. Therefore, a blue shift is observed for the characteristic peaks of the nanoscale Fe_3O_4 in the IR spectrum. In Fig. 3b, the main characteristic peaks of Fe_3O_4/PANI are at 3493, 1584, 1482, 1296, 1215, 1150, 1124, and 803 cm^{-1}. The broad peak near 3493 cm^{-1} corresponds to the N—H stretching vibration in PANI [23]. The 1584 and 1482 cm^{-1} peaks are assigned to the C=C stretching vibrations of N=Q=N (Q = quinone ring) and N—B—N (B = benzene ring), respectively [24]. The 1296 and 1215 cm^{-1} peaks are attributed to the C—N stretching vibrations of the quinone and benzene rings, respectively. The peaks at 1150 and 1124 cm^{-1} are the C—H deformation vibrations in the plane by the sulfosalicylic acid-doped PANI. The 803 cm^{-1} peak is assigned to the =C—H out-of plane deformation vibration of 1,4-para substituted benzene [25,26]. In Fig. 3c, the main characteristic peaks of PANI are at 3493, 1588, 1485, 1296, 1218, 1154, 1124, and 800 cm^{-1}. In Fig. 3b, some peaks are at a lower frequency compared with those in Fig. 3c, indicating that certain chemical bonds are formed between Fe_3O_4 and the PANI backbone. The characteristic peaks of Fe_3O_4 are missing in Fig. 3b, indicating that PANI is polymerized at the Fe_3O_4 particle surface via in situ polymerization.

3.2. Morphological characterization and conductivity analysis of Fe_3O_4, Fe_3O_4/PANI, and PANI

Fig. 4 shows the SEM images of Fe_3O_4, Fe_3O_4/PANI, and PANI. Fe_3O_4 clearly has a spherical morphology, with diameters ranging from 80 nm to 100 nm. Fe_3O_4/PANI appears as a nanorod with a spherical morphology, with diameters between 80 nm and 100 nm. PANI has a one-dimensional nanosheet structure. During polymerization, the aniline monomer is absorbed onto the surface of Fe_3O_4 through electrostatic attraction via the formation of weak charge-transfer complexes between the aniline monomer and the spherical Fe_3O_4 structure. As a result of the absorption process, Fe_3O_4 is coated via the in situ polymerization of the aniline monomer in the presence of Fe_3O_4.

The conductivities of Fe_3O_4, Fe_3O_4/PANI, and PANI are 0.13, 0.30, and 0.24 S cm^{-1}, respectively. Compared with Fe_3O_4/PANI, a superparamagnetic nanorod Fe_3O_4/PANI composite with an average diameter of 80–100 nm has a conductivity of 10^{-2} S cm^{-1} [27]. The crystallinity of Fe_3O_4/PANI is 78.41%, indicating that Fe^{3+}, Fe^{2+}, and O^{2-} ions have higher periodic arrangements in the spinel-type crystal, and the electrons easily transfer from Fe^{2+} to Fe^{3+}. Thus, the Fe_3O_4/PANI material exhibits a higher conductivity of 0.30 S cm^{-1} [28–30].

3.3. Magnetic properties of Fe_3O_4 and Fe_3O_4/PANI

Fig. 5 shows the magnetic hysteresis sample loops of the samples. M_r is defined as the magnetization remaining when the magnetic field is switched off from saturation. H_{ic} is the reverse field required to reduce the magnetization from saturation to zero. For Fe_3O_4 and Fe_3O_4/PANI, the H_{ic} values are 11.65 and 10.18 kA m^{-1}, and the M_r values are 9.09 and 5.27 A m^2 kg^{-1}, respectively. The materials show ferromagnetic properties, which are determined by

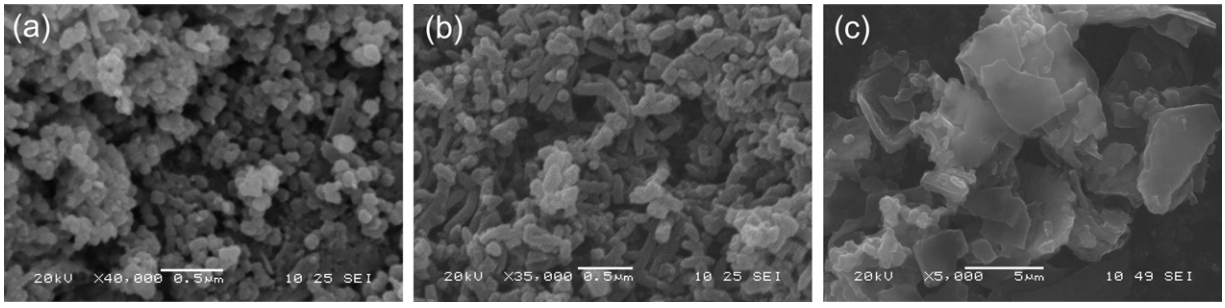

Fig. 4. SEM images of (a) Fe_3O_4, (b) Fe_3O_4/PANI, and (c) PANI.

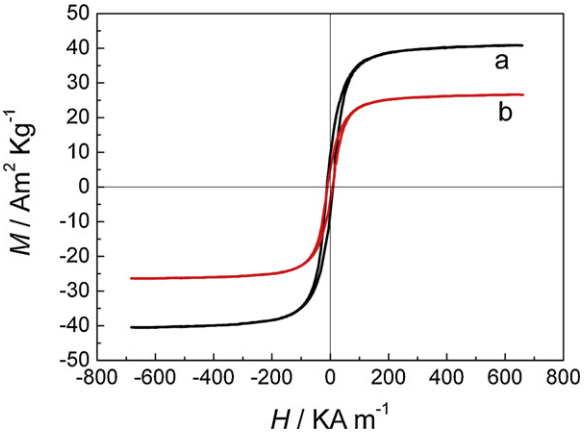

Fig. 5. Hysteresis loops of (a) Fe_3O_4 and (b) Fe_3O_4/PANI.

the magnetic particle sizes and structures. The saturation magnetization of Fe_3O_4/PANI is lower than that of the Fe_3O_4 nanoparticles. The PANI coating on the Fe_3O_4 surface suppresses the magnetic property of the Fe_3O_4 nanoparticles [31].

3.4. Thermal stabilities of PANI and Fe_3O_4/PANI

Fig. 6 shows the TG/DTG/DSC curves of PANI and Fe_3O_4/PANI. In Fig. 6a, the weight loss of PANI can be divided into three main stages. The first stage is below 136.2 °C, with a maximum weight loss of 17.8%. The endothermic peak corresponds to the moisture evaporation in the sample from 95.6 °C to 136.2 °C. The second step, from 136.2 °C to 267.1 °C, is due to the dedoping and decomposition of the sulfosalicylic acid dopant. A 26.9% weight loss is observed from 195.2 °C to 267.1 °C, which is caused by the thermal decomposition of sulfosalicylic acid. Finally, the stage from 267.1 °C to 1200 °C corresponds to PANI glass transition, polymer chain depolymerization, and decomposition. The endothermic peak from 292.7 °C to 370.9 °C is due to the glass transition of PANI. PANI decomposition occurs from 370.9 °C to 1200 °C, with a weight loss rate of −0.104 (% min^{-1}). The total weight loss is 93.92% at 1200 °C. Three weight loss stages are also observed for Fe_3O_4/PANI (Fig. 6b). In the first stage (113.6–156.8 °C), the endothermic peak corresponds to the adsorbed moisture evaporation from the sample, and the weight loss is 9.77% at 156.8 °C. The second stage (228.7–288.4 °C) corresponds to sulfosalicylic acid decomposition, with a weight loss of 19.67%. In the last step, PANI glass transition occurs from 313.6 °C to 413.9 °C, whereas PANI thermal decomposition takes place from 413.9 °C to 1200 °C at a weight loss rate of −0.049 (% min^{-1}).

Compared with the PANI curves, the DSC curve of Fe_3O_4/PANI in Fig. 6b shows no obvious endothermic peak from 313.6 °C to 413.9 °C. At the polymer glass transition temperature ranging from 313.6 °C to 413.9 °C, Fe_3O_4 is oxidized into α-Fe_2O_3 at approximately 400 °C. Therefore, the endothermic and exothermic peaks nearly cancel each other out in this temperature range. At 1140.1 °C, the decrease in thermal power indicates the apparent melting of the Fe_2O_3 nanocrystals. The small size effects significantly lower the melting point of nano Fe_2O_3 to that below the standard melting point (1565 °C). These results clearly indicate that Fe_3O_4 improves the thermal stability of PANI through aniline during in situ polymerization at the surface of the Fe_3O_4 particles. Based on the TG data at 1200 °C, the Fe_3O_4 content in Fe_3O_4/PANI is 22.5% (wt%) [32–35].

Table 1
Electric double-layer capacitance (C_d) and charge-transfer resistance (R_{ct}) of nonmagnetic and magnetic electrodes at different Fe_3O_4/polyaniline (PANI) load densities.

Fe_3O_4/PANI load density (mg cm^{-2})	Nonmagnetic electrode		Magnetic electrode	
	C_d (μF cm^{-2})	R_{ct} (Ω cm^2)	C_d (μF cm^{-2})	R_{ct} (Ω cm^2)
1.20	23.34	0.36	28.20	0.32
3.60	241.77	0.31	612.38	0.47

3.5. Role of Fe_3O_4/PANI during oxygen transfer in a three-electrode electrochemical experiment

The results of the small triangular waveform scanning, multi-current steps, and multi-potential steps are shown in Fig. 7. The Fe_3O_4/PANI load densities are 1.20 and 3.60 mg cm^{-2} in the nonmagnetic and magnetic electrodes, respectively. According to Fig. 7a, the electric double-layer capacitance (C_d) and charge-transfer resistance (R_{ct}) are calculated using Eqs. (1) and (2); the results are listed in Table 1.

$$C_d = \frac{\Delta j_1}{2\nu} \quad (1)$$

$$R_{ct} = \frac{\Delta E}{\Delta j_2} \quad (2)$$

where Δj_1 is the current change at the instant commutation, Δj_2 is the linear current change, ΔE is a linear potential change, and ν is the scan rate (100 V s^{-1}).

Table 1 shows that when the Fe_3O_4/PANI load density is increased from 1.20 mg cm^{-2} to 3.60 mg cm^{-2}, the C_d for both the nonmagnetic and magnetic electrodes increases. At the same load density, the nonmagnetic electrode C_d is smaller than that of the magnetic electrode. However, R_{ct} exhibits a different variation tendency. For the nonmagnetic electrode, R_{ct} is reduced when the load density is increased from 1.20 mg cm^{-2} to 3.60 mg cm^{-2}, whereas a larger R_{ct} at the 3.60 mg cm^{-2} load density is measured for the magnetic electrode. Therefore, the nonmagnetic electrode R_{ct} is larger

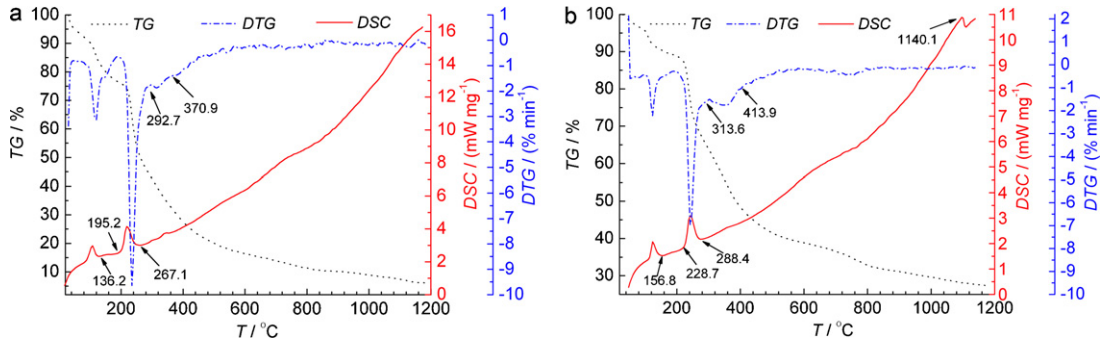

Fig. 6. TG/DTG/DSC analysis results of (a) PANI and (b) Fe_3O_4/PANI.

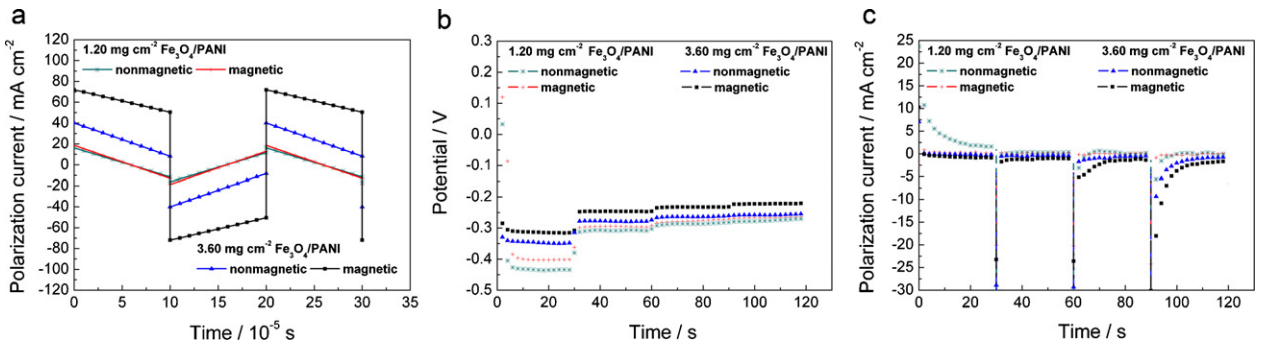

Fig. 7. Electrochemical analyses of the nonmagnetic and magnetic electrodes at different Fe_3O_4/PANI load densities: (a) triangular waveform sweep, (b) multi-current steps, and (c) multi-potential steps.

than that of the magnetic one. However, at the 3.60 mg cm^{-2} load density, R_{ct} is larger for the magnetic electrode.

Fig. 7b shows the potential response of the nonmagnetic and magnetic electrodes to the current steps, with the multi-current steps ranging from −100 mA to −0.1 mA. At the same step current, the reduction potential is increased for both electrodes when the Fe_3O_4/PANI load density is increased, thereby reducing the polarization. At the same Fe_3O_4/PANI load density and step current, the reduction potential of the magnetic electrode is slightly higher than that of the nonmagnetic one. Fig. 7c shows the current response to the potential steps ranging from 1 V to 0.4 V. At the same step potential, the polarization current is increased for both electrodes when the Fe_3O_4/PANI load density is increased. At the same step potential and Fe_3O_4/PANI load density, the polarization current of the magnetic electrode is higher than that of the nonmagnetic one.

Fig. 8 shows the equivalent circuit diagrams of the electrodes. In an unsteady state, when a double-layer charging current (i_c) exists, the electrode parameters are expressed by Eqs. (3)–(6), as follows:

$$Q = \int i_c dt = C_d \eta_c \tag{3}$$

$$i = i_c + i_f \tag{4}$$

$$\eta = \eta_c + \eta_R \tag{5}$$

$$\eta_R = iR_u \tag{6}$$

where Q is the double-layer charging capacity, i_f is the electrochemical reduction reaction current, i is the polarization current, $\eta = |E - E_{equilibrium}|$ is the potential difference or total overpotential, η_c is the electrochemical reaction overpotential, η_R is the electrolyte ohmic overpotential, and R_u is the electrolyte resistance.

As shown in Fig. 7b, the current steps are conducted within a short time. Thus, the electrochemical process of the electrode is performed in an unsteady state. As the current steps instantly occur, the sharp decrease in the reduction potential is caused by the electrolyte ohmic voltage drop, as expressed by Eq. (6). At the same time, the electric double layer is charged by an electric i_c, and the electrochemical reaction is initiated by an electrochemical i_f. For the nonmagnetic electrode, C_d increases as the Fe_3O_4/PANI load density is increased (Table 1). At the same step time, η_c becomes smaller for the electrode with a higher Fe_3O_4/PANI load density

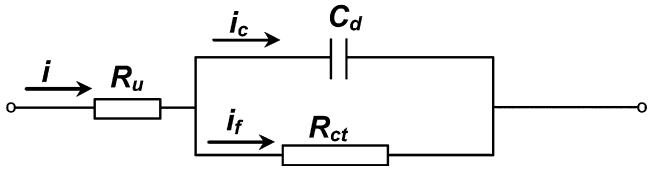

Fig. 8. Equivalent circuit diagrams under a reaction control.

according to Eq. (3). Therefore, the electrode reaches a higher electrochemical reduction potential at the 3.60 mg cm^{-2} load density based on Eqs. (5) and (6). At the same Fe_3O_4/PANI load density, the magnetic electrode has a higher C_d than the nonmagnetic electrode (Table 1). Based on Eqs. (3), (5), and (6), the magnetic electrode has a higher reduction potential than the nonmagnetic electrode at the same step current, indicating that polarization is reduced for the magnetic electrode with the aid of the tiny magnetic field.

The multi-potential steps are also performed within a short time, which also results in an unsteady state for the electrochemical process. As shown in Fig. 7c, as soon as the electrochemical process is initiated, the electric double layer is charged by i_c. According to Eq. (3), the electrode with a higher C_d has a smaller η_c. Thus, from Eq. (5), η_R is larger during the potentiostatic step. Hence, R_u is constant in the three-electrode electrochemical glass cell because R_u is the resistance from the Luggin capillary nozzle to the working electrode surface. Therefore, according to Eq. (6), the polarization current i is larger for the electrode with a higher η_R. As shown in Table 1, the magnetic electrode has a larger C_d than the nonmagnetic electrode at the same Fe_3O_4/PANI load density. This finding explains the larger polarization current of the magnetic electrode (Fig. 7c).

Fig. 9 shows the Tafel curves of the nonmagnetic and magnetic electrodes at different Fe_3O_4/PANI load densities. In Fig. 9a, the Fe_3O_4/PANI load density is 1.20 mg cm^{-2}, and the equilibrium potentials for the nonmagnetic and magnetic electrodes are 0.762 V and 0.785 V (vs. SCE), respectively. At the load density of 3.60 mg cm^{-2} (Fig. 9b), the equilibrium potentials for the nonmagnetic and magnetic electrodes are 0.795 V and 0.761 V (vs. SCE), respectively. At the 1.20 mg cm^{-2} load density, the magnetic electrode clearly has a higher equilibrium potential and higher relative exchange current density than the nonmagnetic electrode. However, at the 3.60 mg cm^{-2} load density, the result is opposite. Both the equilibrium potentials and the relative exchange current densities increase in the nonmagnetic electrode when the Fe_3O_4/PANI load density increases from 1.20 mg cm^{-2} to 3.60 mg cm^{-2}.

Based on Fig. 8, i_c is equal to zero in a steady state or an equilibrium state. Thus, the relationship between η and i_f can be expressed by Eq. (7), as follows:

$$\eta = i_f(R_u + R_{ct}) \tag{7}$$

According to Eq. (7), given the same R_u, a larger R_{ct} corresponds to a greater η at the same i_f under a steady state. In other words, a larger R_{ct} corresponds to a smaller i_f at the same η. The equilibrium state is a peculiar steady state, and when the polarization current i is infinitely close to zero, a larger R_{ct} for an electrode corresponds to a lower equilibrium potential and exchange current density. As shown in Table 1 and Fig. 9a, the magnetic electrode has a smaller R_{ct}, a higher equilibrium potential, and a larger relative exchange current density than the nonmagnetic

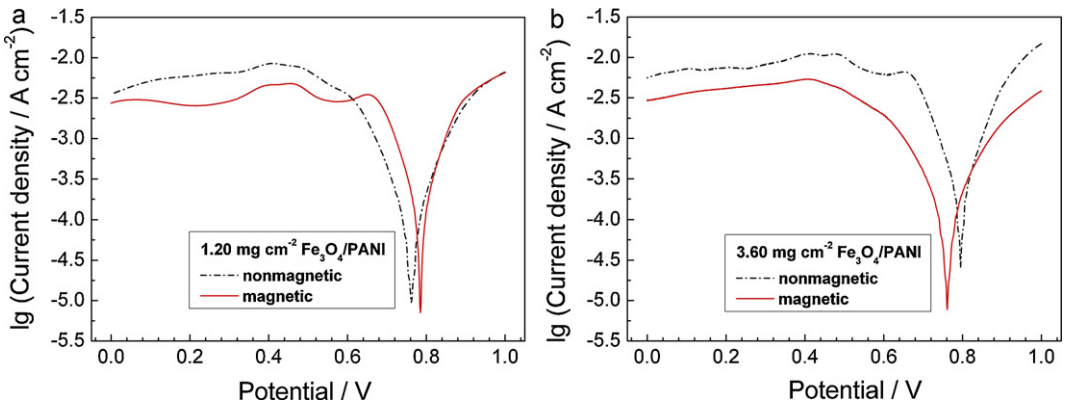

Fig. 9. Tafel curves of the nonmagnetic and magnetic electrodes at (a) 1.20 mg cm^{-2} and (b) 3.60 mg cm^{-2} Fe_3O_4/PANI load densities.

electrode at the 1.20 mg cm^{-2} load density. This finding proves that the tiny magnetic field from Fe_3O_4/PANI promotes oxygen transfer, and that the oxygen reduction reaction easily proceeds under these conditions [36,37]. At the 3.60 mg cm^{-2} load density, the R_{ct} of the magnetic electrode is greater than that of the nonmagnetic electrode (Table 1), whereas the equilibrium potential and the relative exchange current density are lower (Fig. 9b). At the larger Fe_3O_4/PANI load density, the oxygen transfer becomes more disorderly under the irregular tiny magnetic field than under natural convection because of the tiny magnetic field interactions between the different magnetic particles; this phenomenon results in decreased oxygen transfer efficiency. For the nonmagnetic electrode, R_{ct} is reduced when the Fe_3O_4/PANI load density is increased from 1.20 mg cm^{-2} to 3.60 mg cm^{-2} (Table 1), whereas the equilibrium potential and the relative exchange current density increase (Fig. 9). These results indicate that PANI actively participates in the electrochemical reaction through the electrochemical reduction reaction itself, further demonstrating that Fe_3O_4/PANI has a higher conductivity (0.30 S cm^{-1}) and does not cause an obvious ohmic loss in the graphite electrode at a larger load density.

PANI in the magnetic material can increase the C_d [38,39]. At the load density of 1.20 mg cm^{-2}, the magnetic electrode reaches a higher C_d and a lower R_{ct} compared with the nonmagnetic electrode (Table 1). This result indicates that the effects of the tiny magnetic field on oxygen transfer in such an electrochemical process include the promotion of electron transfer, oxygen transfer, and ion alignment in the electric double layer of the electrode [40–43]. A tiny magnetic field can increase C_d, but its effect on R_{ct} is associated with the Fe_3O_4/PANI load density. Oxygen transfer is suppressed by the tiny magnetic field interference at the 3.60 mg cm^{-2} load density. The magnetic field interaction causes the increased R_{ct} between the magnetic poles of different magnetic particles.

3.6. ZAFC discharge performance with Fe_3O_4/PANI in the cathode

The polarization current ratios of the magnetic to the nonmagnetic ZAFC at a discharge voltage of 0.8 V were calculated based on Fig. 10 and listed in Table 2.

As shown in Fig. 10, when the Fe_3O_4/PANI load density in the cathode is less than 3.56 mg cm^{-2}, the magnetic ZAFC has a greater polarization current than the nonmagnetic ZAFC at the same Fe_3O_4/PANI load density. The polarization current ratios are increased with increased Fe_3O_4/PANI load density, as shown in Table 2. This finding further illustrates that the tiny magnetic field from Fe_3O_4/PANI promotes oxygen transfer in the ZAFC cathode. However, when the Fe_3O_4/PANI load density is 7.11 mg cm^{-2}, the discharge performance of the nonmagnetic ZAFC is better than that of the magnetic ZAFC (Fig. 10b), and the polarization current ratio for the magnetic ZAFC is reduced to −0.12. This result demonstrates that the tiny magnetic field differs from that of a macroscopic permanent magnet [3]. At a smaller Fe_3O_4/PANI load density, each magnetic particle forms its own N and S magnetic poles after magnetization, and each magnetic particle forms a closed tiny magnetic field. At the load density of 7.11 mg cm^{-2}, the different magnetic poles of the magnetic particles interact with one other, which can weaken or disturb the tiny magnetic field. The oxygen transfer path can in turn be disrupted by the disorganized magnetic field, thereby decreasing the oxygen transfer efficiency in the tiny magnetic field. As shown in Fig. 10 and Table 2, the polarization current for the nonmagnetic ZAFC increases when the Fe_3O_4/PANI load density in

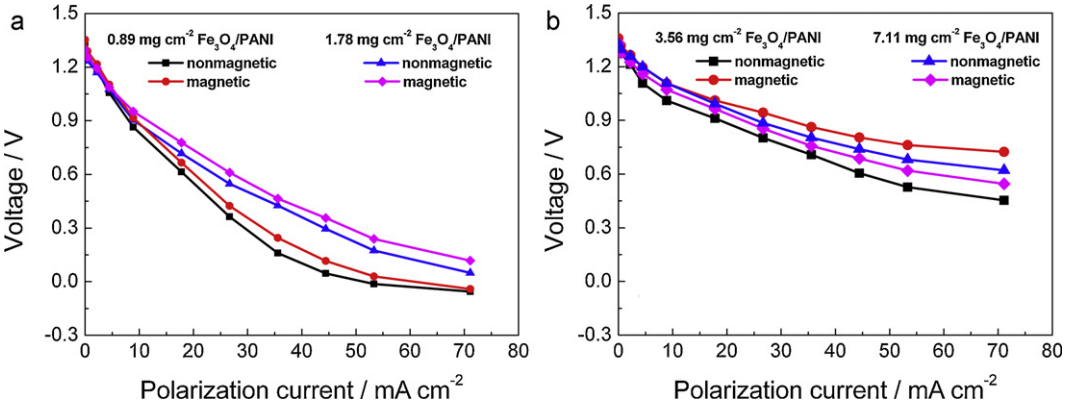

Fig. 10. Polarization curves of the nonmagnetic and magnetic zinc air fuel cell (ZAFC) cathodes with different Fe_3O_4/PANI load densities.

Table 2
Comparison of the polarization current between nonmagnetic and magnetic zinc air fuel cell (ZAFC) cathodes with different Fe_3O_4/PANI load densities at a discharge voltage of 0.8 V.

Fe_3O_4/PANI load density (mg cm^{-2})	Nonmagnetic ZAFC Polarization current, j_a (mA cm^{-2})	Magnetic ZAFC Polarization current, j_b (mA cm^{-2})	Polarization current ratio $(j_b - j_a)/j_a$
0.89	11.22	13.00	0.16
1.78	13.89	16.55	0.19
3.56	26.77	45.20	0.69
7.11	35.87	31.65	−0.12

the cathode is increased, indicating an improved discharge performance. This improvement can be attributed to the participation of PANI in the composites in the cathode electrochemical reduction reaction. PANI also improves the discharge performance of ZAFC. Results show that Fe_3O_4/PANI also has an excellent conductivity. When the Fe_3O_4/PANI load density is increased, the ohmic losses of the ZAFC cathode do not increase.

4. Conclusions

The effect of tiny magnetic fields on oxygen transfer is closely related to properties such as conductivity, magnetic property, and magnetic powder load density on the electrode. The synthesized Fe_3O_4/PANI nanomaterial in the present study has excellent conductivity, high electrochemical reactivity, and ferromagnetic property. Fe_3O_4/PANI plays certain roles during the oxygen transfer process. The tiny magnetic field that Fe_3O_4/PANI generates favors oxygen transfer through oxygen enrichment at the catalytic region. A low Fe_3O_4/PANI load density can ensure an ordered tiny magnetic field, which increases the C_d, decreases the R_{ct}, and improves the discharge performance of ZAFCs. At a high Fe_3O_4/PANI load density, the disordered tiny magnetic field generated by the magnetic field interactions between the magnetic poles of adjacent magnetic particles can weaken the tiny magnetic field. As a consequence, oxygen transfer is inhibited and the discharge performance of ZAFCs decreases.

The tiny magnetic field determines the peculiar applications of the Fe_3O_4/PANI nanomaterials. One potential application area is the button-type ZAFC for small-current discharges. ZAFCs need to be magnetized to improve their performance. The other application area is the mobile high-capacity ZAFC aimed at large-current discharges. This type of ZAFC need not be magnetized, and Fe_3O_4/PANI can take a higher load density in the cathode. Further research on these applications is needed and will be reported in future publications.

Acknowledgments

The authors would like to thank Prof. Xiongfu Zhang and Dr. Yaguang Liu (Dalian university of technology) for their help in some of the experiments. The present research is funded by the National Natural Science Foundation of China (No. 20976018) and the Program for Liaoning Excellent Talents in University (No. 2008RC09).

References

[1] M. Gerard, J.P. Poirot-Crouvezier, D. Hissel, M.C. Pera, Int. J. Hydrogen Energy 35 (2010) 12295–12307.
[2] P. Sapkota, H. Kim, J. Ind. Eng. Chem. 15 (2009) 445–450.
[3] J. Cai, L. Wang, P. Wu, Z.Q. Li, L.G. Tong, S.F. Sun, J. Magn. Magn. Mater. 320 (2008) 171–181.
[4] R. Vijayakumar, Y. Koltypin, I. Felner, A. Gedanken, Mater. Sci. Eng. 286 (2000) 101–105.
[5] W. Zhang, F.L. Shen, R.U. Hong, Particuology 9 (2011) 179–186.
[6] Y. Ling, K. Wei, Y. Luo, X. Gao, S.Z. Zhong, Biomaterials 32 (2011) 7139–7150.
[7] A. Ito, M. Shinkai, H. Honda, T. Kobayashi, J. Biosci. Bioeng. 100 (2005) 1–11.
[8] T. Neuberger, B. Schöpf, H. Hofmann, M. Hofmann, B.V. Rechenberg, J. Magn. Magn. Mater. 293 (2005) 483–496.
[9] H. Wang, R.X. Wang, L. Wang, X.Y. Tian, Colloids Surf. A 384 (2011) 624–629.
[10] G.Y. Li, Y.R. Jiang, K.L. Huang, P. Ding, J. Chen, J. Alloys Compd. 466 (2008) 451–456.
[11] H.Y. Yang, W. Jiang, Y. Lu, Mater. Lett. 61 (2007) 2789–2793.
[12] E. Karaoğlu, A. Baykal, H. Deligöz, M. Şenel, H. Sözeri, M.S. Toprak, J. Alloys Compd. 509 (2011) 8460–8468.
[13] S. Bhadra, D. Khastgir, N.K. Singha, J.H. Lee, Prog. Polym. Sci. 34 (2009) 783–810.
[14] S. Sathiyanarayanan, S. Devi, G. Venkatachari, Prog. Org. Coat. 56 (2006) 114–119.
[15] L. Brožová, P. Holler, J. Kovářová, J. Stejskal, M. Trchová, Polym. Degrad. Stab. 93 (2008) 592–600.
[16] X.C. Wang, S.D. Tang, J. Liu, Z.Q. He, L.J. An, C.X. Zhang, J.M. Hao, W. Feng, J. Nanopart. Res. 11 (2009) 923–929.
[17] T. Jeevananda, J.H. Lee, Siddaramaiah, Mater. Lett. 62 (2008) 3995–3998.
[18] J.p. Yang, Y. Ding, J.K. Zhang, Mater. Chem. Phys. 112 (2008) 322–324.
[19] X.F. Lu, H. Mao, D.M. Chao, W.J. Zhang, Y. Wei, J. Solid State Chem. 179 (2006) 2609–2615.
[20] J.H. Zhou, Z.J. Sui, J. Zhu, P. Li, D. Chen, Y.C. Dai, W.K. Yuan, Carbon 45 (2007) 785–796.
[21] C.L. Lin, C.F. Lee, W.Y. Chiu, J. Colloid Interface Sci. 291 (2005) 411–420.
[22] S. Ahmad, U. Riaz, A. Kaushik, J. Alam, J. Inorg. Organomet. Polym. 19 (2009) 355–360.
[23] P.S. Rao, D.N. Sathyanarayana, S. Palaniappan, Macromolecules 35 (2002) 4988–4996.
[24] S. Yoshimoto, F. Ohashi, T. Kameyama, J. Polym. Sci. B: Polym. Phys. 43 (2005) 2705–2714.
[25] J. Wang, H.F. Xu, J.W. Song, H.J. Zhang, B.L. Gao, Y.D. Huang, J. Mater. Sci. 46 (2011) 2955–2962.
[26] K. Mallick, M.J. Witcomb, M.S. Scurrell, J. Mater. Sci. 41 (2006) 6189–6192.
[27] Z.M. Zhang, M.X. Wan, Synth. Met. 132 (2003) 205–212.
[28] Y.Z. Long, Z.J. Chen, J.L. Duvail, Z.M. Zhang, M.X. Wan, Phys. B (Amst. Neth.) 370 (2005) 121–130.
[29] A.C.V. de Araújo, R.J. de Oliveira, S. Alves Júnior, A.R. Rodrigues, F.L.A. Machado, F.A.O. Cabral, W.M. de Azevedo, Synth. Met. 160 (2010) 685–690.
[30] W.Y. Xue, K. Fang, H. Qiu, J. Li, W.M. Mao, Synth. Met. 156 (2006) 506–509.
[31] W. Shen, M.M. Shi, M. Wang, H.Z. Chen, Mater. Chem. Phys. 122 (2010) 588–594.
[32] J.C. Aphesteguy, S.E. Jacobo, J. Mater. Sci. 42 (2007) 7062–7068.
[33] N. Pinna, S. Grancharov, P. Beato, P. Bonville, M. Antonietti, M. Niederberger, Chem. Mater. 17 (2005) 3044–3049.
[34] Z.A. Hu, H.X. Zhao, C. Kong, Y.Y. Yang, X.L. Shang, L.J. Ren, Y.P. Wang, J. Mater. Sci. 17 (2006) 859–863.
[35] J.J. Ma, X.B. Zhang, C. Yan, Z.W. Tong, H. Inoue, J. Mater. Sci. 43 (2008) 5534–5539.
[36] T. Okada, N.I. Wakayama, L.B. Wang, H. Shingu, J.I. Okano, T. Ozawa, Electrochim. Acta 48 (2003) 531–539.
[37] J.H. Zeng, S.J. Liao, J.Y. Lee, Z.X. Liang, Int. J. Hydrogen Energy 35 (2010) 942–948.
[38] W.C. Chen, T.C. Wen, H. Teng, Electrochim. Acta 48 (2003) 641–649.
[39] B. Gupta, R. Prakash, Mater. Sci. Eng. Proc. Conf. 29 (2009) 1746–1751.
[40] K.T. Chang, C.I. Weng, Comput. Mater. Sci. 43 (2008) 1048–1055.
[41] I. Bica, J. Ind. Eng. Chem. 15 (2009) 605–609.
[42] R. Sueptitz, J. Koza, M. Uhlemann, A. Gebert, L. Schultz, Electrochim. Acta 54 (2009) 2229–2233.
[43] S. Aoyagi, A. Yano, Y. Yanagida, E. Tanihira, A. Tagawa, M. Iimoto, Chem. Phys. 331 (2006) 137–141.